



Effects of Cr and Fe Addition on Microstructure and Tensile Properties of Ti–6Al–4V Prepared by Direct Energy Deposition

Yool Byun^{1,3} · Sangwon Lee¹ · Seong-Moon Seo² · Jong-taek Yeom¹ · Seung Eon Kim¹ · Namhyun Kang³  · Jaekeun Hong¹ 

Received: 17 April 2018 / Accepted: 15 May 2018 / Published online: 29 June 2018
© The Korean Institute of Metals and Materials 2018

Abstract

The effects of Cr and Fe addition on the mechanical properties of Ti–6Al–4V alloys prepared by direct energy deposition were investigated. As the Cr and Fe concentrations were increased from 0 to 2 mass%, the tensile strength increased because of the fine-grained equiaxed prior β phase and martensite. An excellent combination of strength and ductility was obtained in these alloys. When the Cr and Fe concentrations were increased to 4 mass%, extremely fine-grained martensitic structures with poor ductility were obtained. In addition, Fe-added Ti–6Al–4V resulted in a partially melted Ti–6Al–4V powder because of the large difference between the melting temperatures of the Fe eutectic phase (Ti–33Fe) and the Ti–6Al–4V powder, which induced the formation of a thick liquid layer surrounding Ti–6Al–4V. The ductility of Fe-added Ti–6Al–4V was thus poorer than that of Cr-added Ti–6Al–4V.

Keywords Ti–6Al–4V alloy · Alloying elements · Strengthening · Partially melted powder · Direct energy deposition

1 Introduction

Laser-based metal 3D printing can be divided into selective laser melting (SLM) and direct energy deposition (DED). In SLM, a metal powder is filled in the entire area of the target layer, and the laser melts the powder. The resulting net-shaped product is advantageous for additive manufacturing, and the product samples can be formed in complex shapes [1]. However, the SLM process has a disadvantage in that the process duration is relatively long because a controlled atmosphere is employed in

the chamber. In the DED process, a sample is fabricated while a laser is simultaneously jetted with a powder, and the laser power is relatively high. Although the building speed is fast, the net shape of the DED sample is poor, so machining processes such as surface treatment are required. During DED, the shielding gas is sprayed and deposited without controlling the atmosphere as a whole, which is advantageous because it can be used for producing and repairing a large product [2]. This type of additive manufacturing has been studied to prepare various alloys, including Ni-based superalloys and stainless steel [3, 4]. Many studies using titanium alloys have also been carried out for the manufacture of aerospace components with additive manufacturing (AM) [5]. Since titanium is expensive and difficult to manipulate during the deformation process, the buy-to-fly ratio is low. Applying titanium to additive manufacturing can greatly increase the buy-to-fly ratio and thus decrease the production cost. Among the titanium alloys, Ti–6Al–4V alloys have especially good mechanical properties and have been extensively studied as a result [6, 7].

When DED is carried out on a Ti–6Al–4V alloy, coarse prior β grains are formed with the martensite phase owing to the high cooling rate during deposition. The strength of the processed alloy is higher than that of wrought

✉ Namhyun Kang
nhkang@pusan.ac.kr

✉ Jaekeun Hong
jkhong@kims.re.kr

¹ Advanced Metals Division, Titanium Alloys Department, Korea Institute of Materials Science (KIMS), Changwon 51508, Republic of Korea

² High Temperature Materials Center, Korea Institute of Materials Science (KIMS), Changwon 51508, Republic of Korea

³ Department of Materials Science and Engineering, Pusan National University, Busan 46241, Republic of Korea

Ti–6Al–4V, but the ductility is low, which limits its practical application. It is known that adding alloying elements to Ti–6Al–4V can form fine and equiaxed β grains. Martin et al. [8] have developed a successful process to produce crack-free fine equiaxed grain structure by adding Zr as an alloying element to the Al7075 alloy with selective laser melting. Attempts have also been made to add a β stabilizer such as Mo to the DED process of titanium alloys [9]. It was reported that the size of the prior grains in Ti–6Al–4V alloys can be controlled by adding Cr and Fe as alloying elements [10].

When a mixed Ti–6Al–4V–M powder is subjected to the DED process, its strength and prior β grains can be controlled. However, there have been very few studies on the deposition of a mixed Ti–6Al–4V–M powder in additive manufacturing. The addition of Cr and Fe during DED is expected to improve the low ductility of the Ti–6Al–4V alloy. In this study, the effects of the addition of alloying elements (2 and 4 mass% of Cr and Fe powders) on the mechanical properties and microstructure of the Ti–6Al–4V alloy were investigated.

2 Experimental Procedures

The baseplate used for deposition in the present study was made of a Ti–6Al–4V alloy. Three powders were used as the starting materials—Ti–6Al–4V powder with 99.9% purity, Cr powder with 99% purity, and Fe powder with 99.9% purity. As shown in Fig. 1, the Ti–6Al–4V alloy powder particles had a completely spherical shape, and the Cr and Fe powder particles had an irregular shape. The composition of the Ti–6Al–4V powder is shown in Table 1. The average powder diameter of Ti–6Al–4V, Cr and Fe are 111.6, 78.8 and 64.8 μm , respectively. All of powders were sieved in order to improve flow rate. These powders used in the experiment were mixed for 1 h with a two-axis rotation tool.

The deposition method used in the DED process is illustrated in Fig. 2, and all of the samples were deposited under the same conditions. Contours were deposited at the beginning and the end, and a pocket was deposited in the middle of the process. The pocket was used to alternately stack the odd- and even-numbered pattern layers shown in Fig. 2. The sample was designed to have a rectangular shape with dimensions of $8 \times 8 \times 45$ mm. The layer thickness (L) and

Fig. 1 SEM images of powders: **a** Ti–6Al–4V (regular shape), **b** chromium (irregular shape), and **c** iron (irregular shape)

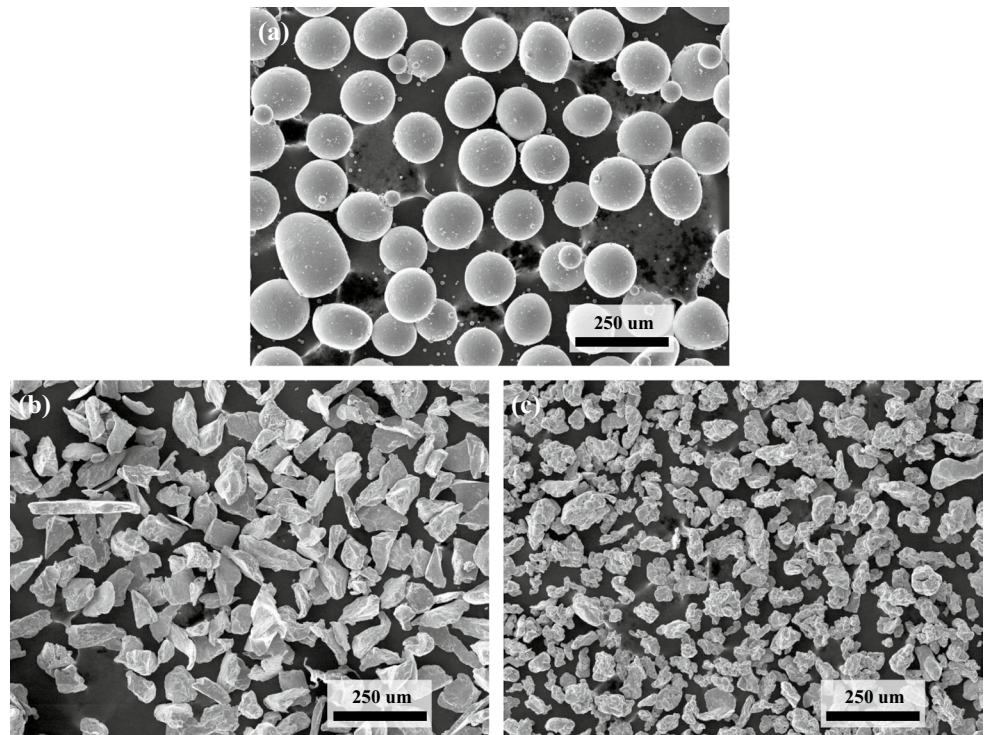


Table 1 Chemical composition of Ti–6Al–4V powder

wt%	Ti	Al	V	Fe	O	Other
Ti–6Al–4V	Balance	6.44	4.0	0.21	0.1	<0.4

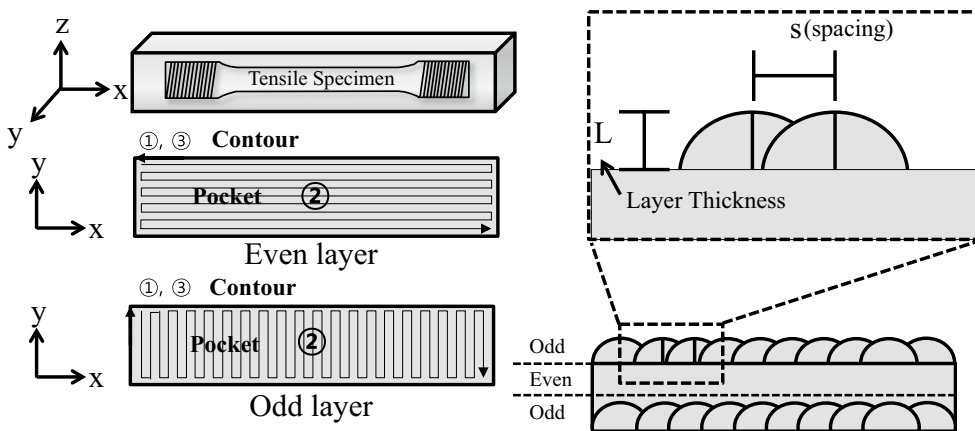


Fig. 2 Schematic diagrams to indicate scanning pattern and experimental parameters of DED process

the spacing (*s*) were set at 0.25 and 0.5 mm, respectively. The laser used in the experiments was a 2 kW Nd–YAG laser from IPG Photonics (USA), and it had a spot diameter of 0.8 mm. The optimum operating settings of the laser for deposition were a power of 350 W and a scanning speed of 0.85 m/min. The deposition process was carried out with flows of powder gas at 2 L/min, coaxial gas at 9 L/min, and shielding gas at 5 L/min. The alloy powder was distributed at a rate of 1.5 g/min.

Three tensile tests were carried out for every alloy sample. ASTM E8M tensile specimens with a gauge length of 12.5 mm were machined from fabricated samples. The tensile axis is aligned parallel to x axis shown in Fig. 2. The tensile test was conducted at a speed of 10^{-3} /s. The hardness was measured using a Vickers hardness tester with a load of 0.5 kgf. The microstructure was examined, and energy-dispersive X-ray spectroscopy (EDS) analysis was carried out after the specimens were mechanically polished and etched in a Kroll solution ($96 \text{ H}_2\text{O} + 2 \text{ HF} + 2 \text{ HNO}_3$). For electron-backscatter diffraction (EBSD) analysis and electron probe

micro-analyzer (EPMA), mechanical polishing was performed using ≤ 800 grit paper, followed by electro-polishing with a solution consisting of 50% CH_3OH , 42.5% $\text{C}_2\text{H}_6\text{O}_2$, and 7.5% HClO_4 . The EBSD used a working distance of 18 mm, a voltage of 15 kV, and a step size of 0.2 μm . The average of confidence index was 0.79. The operating settings of EPMA were a voltage of 15 kV, a dwell time of 20 ms, and a probe diameter with circle shape of 0.3 μm .

3 Results and Discussion

Figure 3 shows the tensile properties of Ti–6Al–4V; Cr-added Ti–6Al–4V, hereafter referred to as Ti–6Al–4V–(Cr); and Fe-added Ti–6Al–4V, hereafter referred to as Ti–6Al–4V–(Fe). The original Ti–6Al–4V alloy showed an ultimate tensile strength (UTS) of 970 MPa and an elongation of 5%. As the Cr and Fe content was increased, the tensile strength of the modified alloys increased: the Ti–6Al–4V–4Cr and Ti–6Al–4V–4Fe alloys

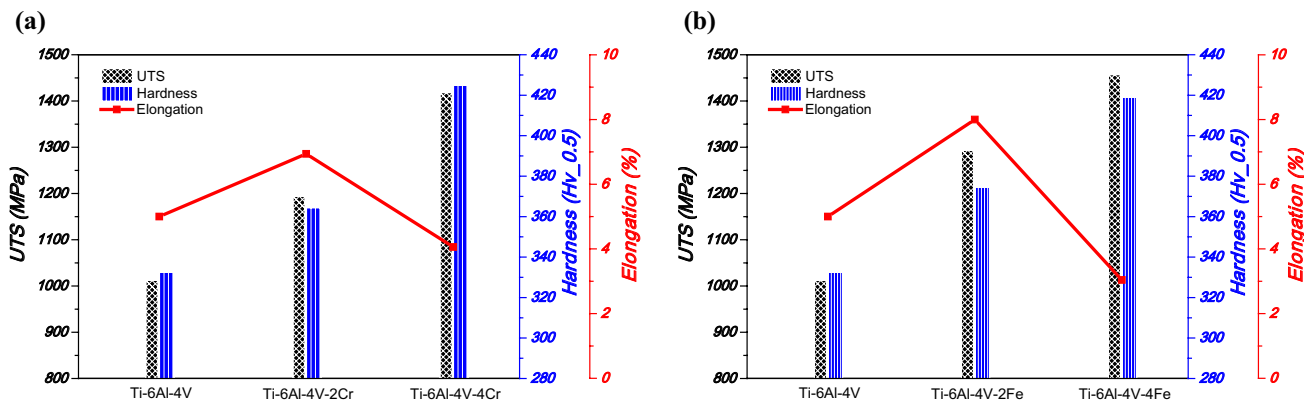


Fig. 3 Effect of a Cr and b Fe composition on the mechanical properties of Ti–6Al–4V alloys

exhibited UTS of 1418 and 1457 MPa, respectively. The Cr and Fe additions on hardness showed same trend and it can be seen that the hardness increases with increasing the Cr and Fe additions (Fig. 3). The total elongation increased as the Cr and Fe concentrations were increased to 2 mass%, while it decreased when the Cr and Fe concentrations were about 4 mass%.

Figure 4 shows optical micrographs of the Ti-6Al-4V-(Cr, Fe) prepared by DED process. The Ti-6Al-4V alloy consisted of α and α' phases within the coarse columnar-grained prior β phase. As reported in the literature [11, 12], Ti-6Al-4V alloy made of AM normally has a fully columnar structure. The addition of Fe and Cr to titanium alloys resulted in constitutional undercooling at the solid/liquid interface during solidification and this may facilitate the formation of fine equiaxed prior β grains [13]. Some of black particles (Fig. 4c, e) were observed in the

Ti-6Al-4V-(Fe) alloys, whereas few traces of particles were observed in the Ti-6Al-4V-(Cr) alloys.

In order to identify the black particles shown in Fig. 4c, e, EPMA mapping was conducted in DED processed Ti-6Al-4V alloy. Figure 5 shows the SEM and Fe elemental mapping micrographs of this particle. It can be seen that the particle has a spherical shape and shows low Fe content. The particles had no Fe content (Ti-6Al-4V) while the average Fe content of matrix was about 3.26 mass%. The result reveals that Fe addition induces partially melted Ti-6Al-4V powder and the powder diameter decreases less than the initial diameter. It appears that these partially melted particles could act as defects and hence reduce the elongation of DED processed Ti-6Al-4V-4Fe alloy.

It is essential to understand the solidification process in order to predict the microstructural evolution during SLM and DED processes. Figure 6 shows the solidification map

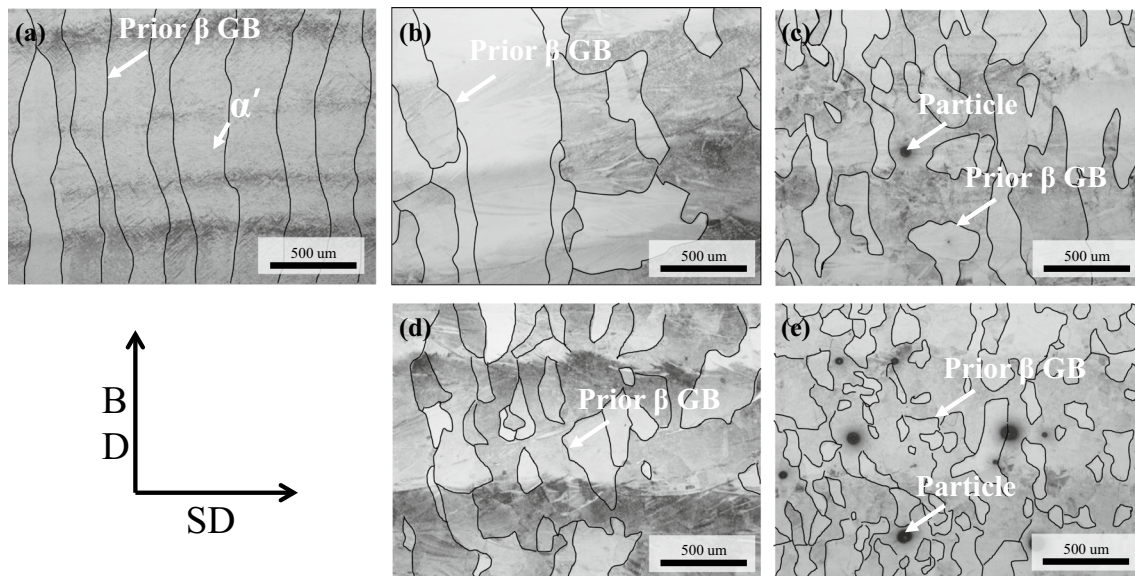


Fig. 4 Optical microstructures of the DED specimens: **a** Ti-6Al-4V, **b** Ti-6Al-4V-2Cr, **c** Ti-6Al-4V-2Fe, **d** Ti-6Al-4V-4Cr, and **e** Ti-6Al-4V-4Fe

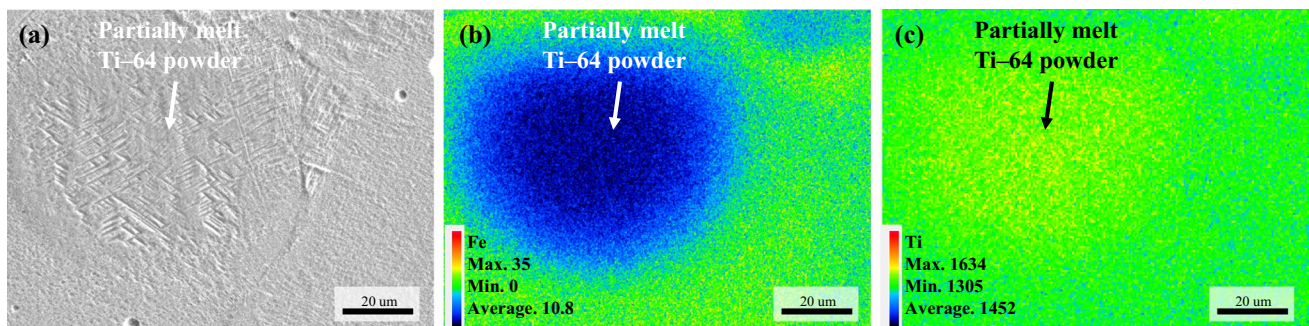


Fig. 5 The partially melted Ti-6Al-4V powders in Ti-6Al-4V-4Fe sample: **a** SEM image, **b** Fe mapping, and **c** Ti mapping

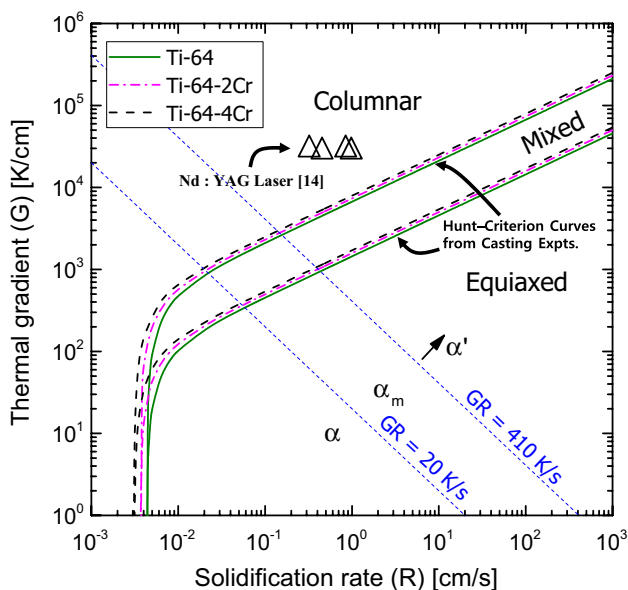


Fig. 6 The Ti–6Al–4V solidification map showing effect of Cr addition on Hunt–Criterion curve of Ti–6Al–4V alloy and Nd:YAG deposition of G and R values [11, 14, 16, 18]

of Ti–6Al–4V alloy, which is suggested by Kobryn and Semiatin [14]. Figure 6 also shows the temperature gradient (G) and solidification rate (R) conditions of Nd:YAG laser processed Ti–6Al–4V alloy [15], which is similar to the present experimental conditions [16, 17]. As the laser power increases, the position of the plot shifts downward. As the scan speed increases, the position of the plot moves to the upper right direction. The solid lines in Fig. 6 represent experimentally determined boundary lines between columnar and equiaxed grain morphologies of Ti–6Al–4V alloy based on the Hunt’s columnar to equiaxed transition (CET) model [18]. According to Hunt’s CET model, fully equiaxed grain structure is obtained by Eq. (1):

$$G < 0.617N_0^{1/3} \left\{ 1 - \frac{(\Delta T_N)^3}{(\Delta T_c)^3} \right\} \Delta T_c \tag{1}$$

where G is the temperature gradient, N_0 is the number of nucleation sites, ΔT_N is the undercooling at the heterogeneous nucleation temperature, and ΔT_c is the undercooling equal to that of the columnar growth front temperature. In the meantime, the solidification structure is fully columnar when

$$G > 0.617(100N_0)^{1/3} \left\{ 1 - \frac{(\Delta T_N)^3}{(\Delta T_c)^3} \right\} \Delta T_c \tag{2}$$

Based on Hunt’s analytical method [18], it is assumed that the undercooling of the growing dendrite is simplified into

$$\Delta T = \left(\frac{V' C_0}{A} \right)^{1/2} \tag{3}$$

V' is the real interface velocity, C_0 is the initial solute concentration and A is the constant. It is assumed that Eq. (3) applies for the growing dendrite with both the columnar and the equiaxed morphologies. The effect of Cr additions on the CET of Ti–6Al–4V alloy is calculated using Eqs. (1–3) and is presented in Fig. 6 with a dashed dotted line (Ti–6Al–4V–2Cr) and dashed line (Ti–6Al–4V–4Cr). It can be seen in Fig. 6 that no significant change is observed with an addition of alloying elements in Ti–6Al–4V alloy. However, microstructural observations of these alloys clearly showed that the morphology of prior β grains changes from fully columnar to equiaxed with increasing alloying additions in Fig. 4b–e. These results indicate that increasing the undercooling of dendrite tip by the addition of alloying elements is not a critical factor to facilitate the growth of equiaxed β grains during DED process. Instead, it appears that Cr and Fe additions would significantly increase the nucleation sites and thus promote the formation of equiaxed β grains during solidification. It should be also mentioned that the partially melted Ti–6Al–4V powder during DED process could act as crucial heterogeneous nucleation sites of β grains. As reported by Wang et al. [19], partially melted powders could provide additional nucleation sites within the local melt pool and thus lead to the formation of equiaxed grains during laser melting deposition additive manufacturing of titanium alloys. However, it appears that further work is needed in order to clarify the effect of partially melted powders on increasing the heterogeneous nucleation sites.

Figure 7 shows the EBSD results of the Ti–6Al–4V–(Cr, Fe) alloys. The orange and green colors represent the α and β phases, respectively. As the Cr and Fe content increased, the volume fraction of the remaining β phase increased. This can be explained by the molybdenum equivalent, which can be presented by Eq. (4) [20]:

$$[\text{Mo}]_{\text{eq}} = [\text{Mo}] + 1/5[\text{Ta}] + 1/3.6[\text{Nb}] + 1/2.5[\text{W}] + 1/1.5[\text{V}] + 1.25[\text{Cr}] + 1.25[\text{Ni}] + 1.6[\text{Mn}] + 1.7[\text{Co}] + 2.5[\text{Fe}] \tag{4}$$

The value of the molybdenum equivalent represents the effects of alloying elements on the stability of the β phase. As the molybdenum equivalent increased, the martensite transformation was inhibited and volume fraction of retained β increased [21]. Table 2 shows the phase fraction and molybdenum equivalent of Ti–6Al–4V–(Cr, Fe) alloys. It can be seen that the high β stability decreased the grain size of martensite. The martensite in the Ti–6Al–4V–4(Cr, Fe) alloys was extremely fine, which could result in high strength (> 1400 MPa) but poor ductility (< 5%).

Figure 8 shows the fracture surface of Ti–6Al–4V–(Cr, Fe) alloys after the tensile tests. The Ti–6Al–4V, Ti–6Al–4V–2Cr, and Ti–6Al–4V–4Cr samples showed the

coexistence of dimples and quasi-cleavage facet, but the Ti–6Al–4V–2Fe and Ti–6Al–4V–4Fe samples exhibited brittle fracture around the pores generated by the partially

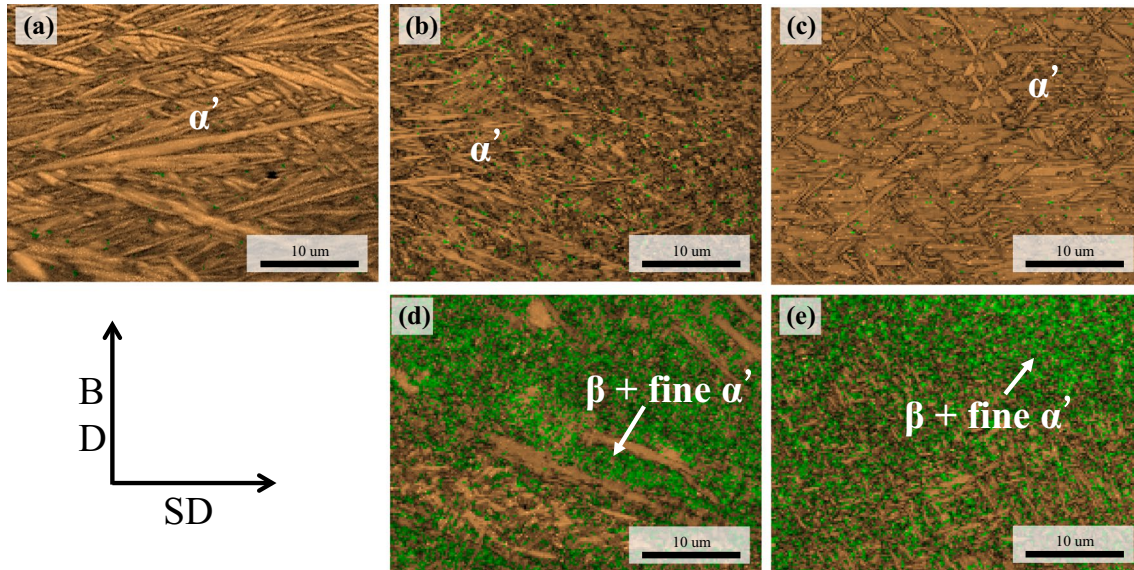


Fig. 7 Effect of Cr and Fe composition on EBSD phase maps: **a** Ti–6Al–4V, **b** Ti–6Al–4V–2Cr, **c** Ti–6Al–4V–2Fe, **d** Ti–6Al–4V–4Cr, and **e** Ti–6Al–4V–4Fe

Table 2 Phase fraction and molybdenum equivalent of each alloy

	Ti–6Al–4V	Ti–6Al–4V–2Cr	Ti–6Al–4V–2Fe	Ti–6Al–4V–4Cr	Ti–6Al–4V–4Fe
α	99.5	96.8	99.2	62.1	62.0
β	0.5	3.2	0.8	37.9	38.0
$[\text{Mo}]_{\text{eq}}$	2.68	5.68	7.68	7.68	12.68

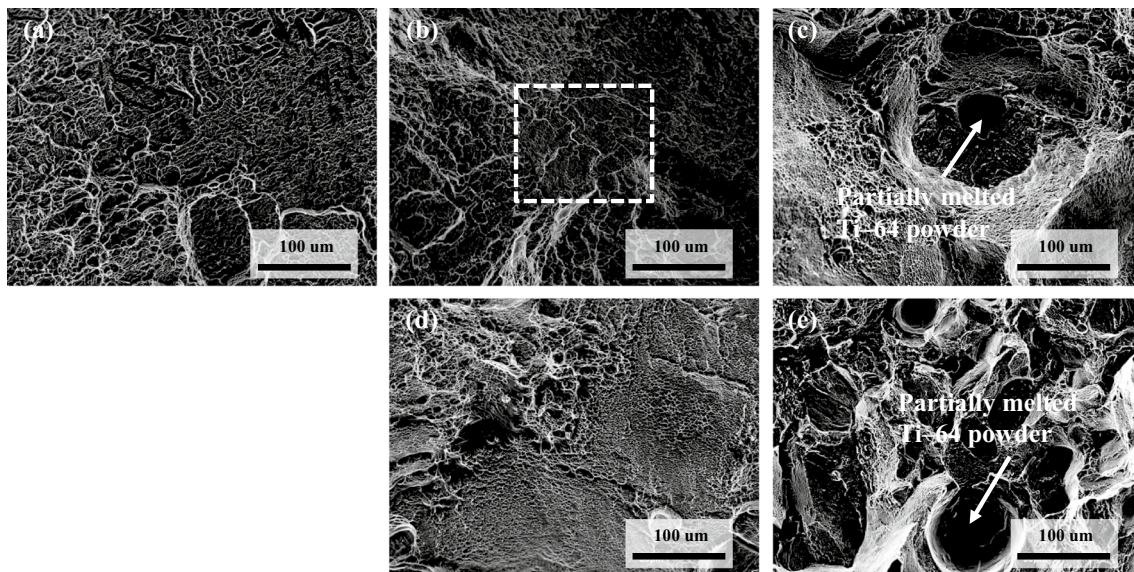


Fig. 8 Effect of Cr and Fe composition on SEM fractography: **a** Ti–6Al–4V, **b** Ti–6Al–4V–2Cr, **c** Ti–6Al–4V–2Fe, **d** Ti–6Al–4V–4Cr, and **e** Ti–6Al–4V–4Fe

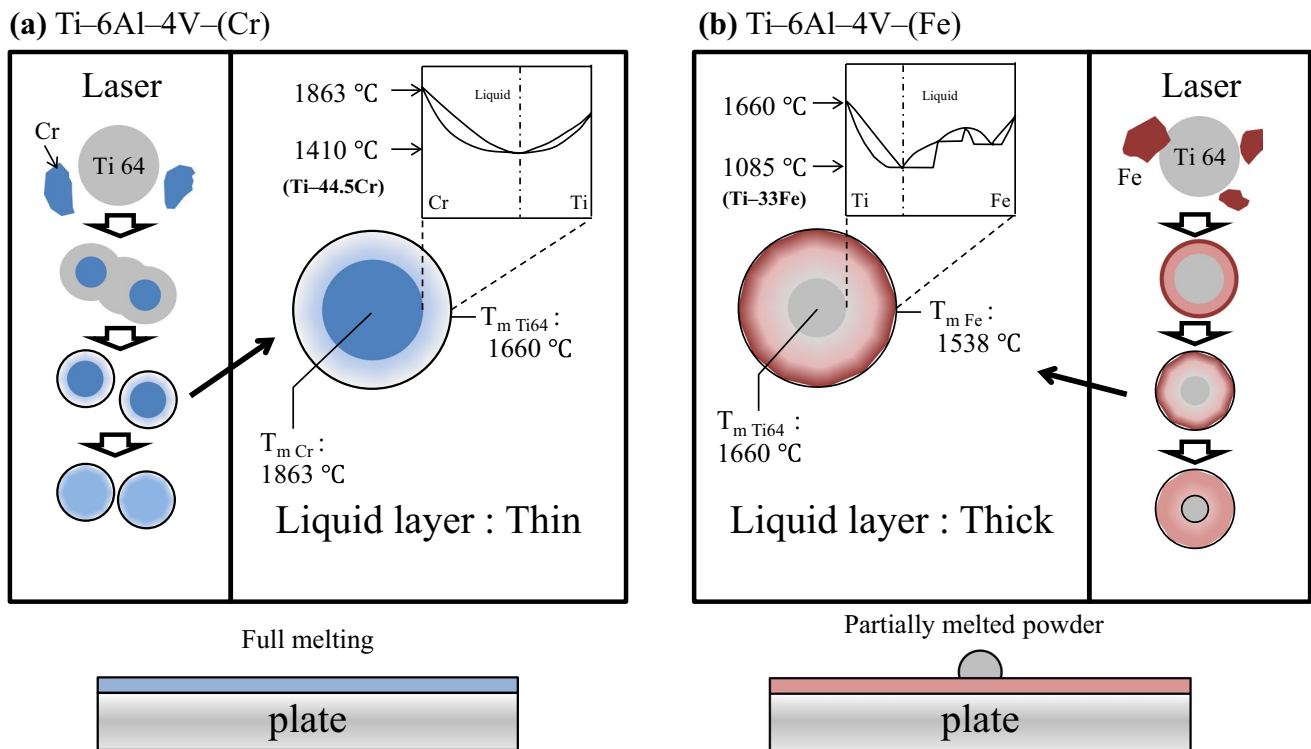


Fig. 9 Schematic melting procedure of **a** Ti-6Al-4V-(Cr) and **b** Ti-6Al-4V-(Fe) mixed powder during laser exposure

melted powders as shown in Fig. 4c, e. These results reveal that the existence of the partially melted powders reduced the ductility. Overall, the Ti-6Al-4V-(Fe) alloys showed poor ductility when compared to the Ti-6Al-4V-(Cr) alloys.

Figure 9 schematically illustrates the melting behavior of Ti-6Al-4V-(Cr, Fe) powders. The left side of each panel shows the melting process of a mixed powder upon exposure to laser irradiation; the right side of each panel shows an illustration of the middle stage of melting. Since the wettability of the Ti-6Al-4V surface by the Cr and Fe liquids was high [22], the powder could be instantaneously enclosed by the liquid upon dissolution. In the case of the Ti-6Al-4V-(Cr) powder, because the melting point of Cr is higher than that of Ti-6Al-4V, Ti-6Al-4V melted first and encapsulated the Cr powder. When the eutectic composition (Ti and 44.5 mass% Cr) was formed around the Cr powder enclosed by Ti-6Al-4V, the melting point was reduced to approximately 300 °C below that of the Ti-6Al-4V powder. Since the layer depth was relatively low, the sphere could be uniformly melted because the temperature difference between the inside and the outside was small. In the case of the Ti-6Al-4V-(Fe) powder, because Fe has a lower melting point than the Ti-6Al-4V alloy, Fe melted first and the Fe liquid encapsulated the Ti-6Al-4V powder. When the eutectic composition (Ti and 33 mass% Fe) was formed around the Ti-6Al-4V powder that was surrounded by the Fe liquid, a flux could

be formed at a temperature below 1085 °C inside the powder. Since the liquid phase of the metal has a higher specific heat capacity than that of the solid phase, heating the dissolved liquid phase at lower temperatures requires more heat. A thick liquid layer was thus formed on the surface of Ti-6Al-4V. As a result, the Ti-6Al-4V powder was protected by the thick liquid layer, and the partially melted Ti-6Al-4V powder could finally remain on the plate. Because outer layer of Ti-6Al-4V powder was partially melted by the eutectic reaction, the diameter of the un-melted powder was smaller than that of the initial Ti-6Al-4V powder. This hypothesis is justified by the observed result showing that average powder particle of un-melted powder was approximately 58 μm which was 51.8% smaller than that of initial Ti-6Al-4V powder with d_{50} particle size of 111.6 μm.

4 Conclusions

The effects of Cr and Fe addition on the mechanical properties of Ti-6Al-4V prepared by DED were investigated. The main conclusions are as follows:

1. As the Fe and Cr content was increased from 0 to 2 mass%, the morphology of the prior β phase started

to change from coarse-grained columnar structures to fine-grained equiaxed structures. The partially melted Ti–6Al–4V powder acted as heterogeneous nucleation site, it caused the equiaxed prior β grain rather than compositional effect. The equiaxed prior β phase consisted of the α phase and fine martensite, which exhibited an excellent combination of strength and ductility.

2. As the Fe and Cr content was increased from 2 to 4 mass%, a fine-grained and fully equiaxed prior β phase was observed. The martensite in the prior β phase was extremely fine. This martensitic structure resulted in very high strength (> 1.4 GPa), but poor ductility ($< 5\%$).
3. The micrographs of the Ti–6Al–4V–(Fe) alloys show the presence of partially melted powders, whereas there was no trace of powder in the Ti–6Al–4V–(Cr) alloys because the difference between the melting temperatures of the Fe eutectic phase (Ti–33Fe) and the Ti–6Al–4V powder was much larger than that between the Cr eutectic phase (Ti–44.5Cr) and the Ti–6Al–4V powder. This large temperature difference resulted in the formation of the thick liquid layer surrounding the Ti–6Al–4V powder that prevented it from melting (shielding phenomenon).

Acknowledgements This study was supported by the Ministry of Trade, Industry and Energy (Grant No. 10077677) and supported by grants from the Fundamental Research Program (PNK5520) of the Korea Institute of Materials Science.

References

1. S. Zhang, X. Lin, J. Chen, W. Huang, *Chin. Opt. Lett.* **7**, 498–501 (2009)
2. L. Yang, K. Hsu, B. Baughman, D. Godfrey, F. Medina, M. Menon, S. Wiener, *Additive Manufacturing of Metals: The Technology, Materials, Design and Production* (Springer, London, 2017), p. 24
3. F. Caiazzo, *Opt. Laser Technol.* **103**, 193–198 (2018)
4. K. Zhang, S. Wang, W. Liu, X. Shang, *Mater. Des.* **55**, 104–119 (2014)
5. B. Baufeld, O.V.D. Biest, R. Gault, *Mater. Des.* **31**, S106–S111 (2010)
6. J. Yu, M. Rombouts, G. Maes, F. Motmans, *Phys. Proc.* **39**, 416–424 (2012)
7. B.J. Hayes, B.W. Martin, B. Welk, S.J. Kuhr, T.K. Ales, D.A. Brice, I. Ghamarian, A.H. Baker, C.V. Haden, D.G. Harlow, H.L. Fraser, P.C. Collins, *Acta Mater.* **133**, 120–133 (2017)
8. J.H. Martin, B.D. Yahata, J.M. Hundley, J.A. Mayer, T.A. Schae-dler, T.M. Pollock, *Nature* **549**, 365–369 (2017)
9. C. Schneider-Maunoury, L. Weiss, P. Acquier, D. Boisselier, P. Laheurte, *Addit. Manuf.* **17**, 55–66 (2017)
10. Y. Itoh, H. Miura, T. Uematsu, T. Osada, K. Sato, *J. Solid Mech. Mater. Eng.* **3**, 921–930 (2009)
11. T. Ahmed, H. Rack, *Mat. Sci. Eng. A* **243**, 206–211 (1998)
12. Y. Ren, X. Lin, X. Fu, H. Tan, J. Chen, W. Huang, *Acta Mater.* **132**, 82–95 (2017)
13. M.J. Bermingham, S.D. McDonald, M.S. Dargusch, D.H. StJohn, *Mater. Sci. Forum* **654–656**, 1472–1475 (2010)
14. P.A. Kobryn, S.L. Semiatin, *J. Mater. Proc. Tech.* **135**, 330–339 (2003)
15. S. Bontha, N.W. Klingbeil, P.A. Kobryn, H.L. Fraser, *J. Mater. Proc. Tech.* **178**, 135–142 (2006)
16. J. Hunt, *Mater. Sci. Eng.* **65**, 75–83 (1984)
17. M. Yan, P. Yu, *Sintering Techniques of Materials* (IntechOpen, 2015)
18. P.A. Kobryn, S.L. Semiatin, *JOM* **53**, 40–42 (2001)
19. T. Wang, Y.Y. Zhu, S.Q. Zhang, H.B. Tang, H.M. Wang, *J. Alloy. Compd.* **632**, 505–513 (2015)
20. R.R. Boyer, G.E. Welsch, E.W. Collings (eds.), *Materials Properties Handbook: Titanium Alloys* (ASM International, Materials Park, 1994), p. 10
21. C. Leyens, M. Peters, *Titanium and Titanium Alloys* (Wiley, New York, 2003)
22. U. Diebold, *Surf. Sci. Rep.* **48**, 53–229 (2003)